JACS Au
AN OPEN ACCESS JOURNAL OF THE AMERICAN CHEMICAL SOCIETY

pubs.acs.org/jacsau
Article

Electrical Conductivities and Conduction Mechanism of Lithium-Doped High-Entropy Oxides at Different Temperature and Pressure Conditions

Meng Song, Xiaoliang Zhang, Shun Wan, Gui Wang, Junxiu Liu, Weiwei Li, Hongliang Dong, Chenjie Lou, Zhiqiang Chen, Bin Chen, and Hengzhong Zhang*

Cite This: JACS Au 2024, 4, 592−606
Read Online

ACCESS | Metrics & More | Article Recommendations | Supporting Information

ABSTRACT: Li-doped high-entropy oxides (Li-HEO) are promising electrode materials for Li-ion batteries. However, their electrical conduction in a wide range of temperatures and/or at high pressure is unknown, hindering their applications under extreme conditions. Especially, a clear understanding of the conduction mechanism is needed. In this work, we determined the carrier type of several Li-doped (MgCoNiCuZn)O semiconductor compounds and measured their electrical conduction at temperatures 79−773 K and/or at pressures up to 50 GPa. Three optical band gaps were uncovered from the UV−vis−NIR absorption measurements, unveiling the existence of defect energy levels near the valence band of p-type semiconductors. The Arrhenius-like plot of the electrical conductivity data revealed the electronic conduction in three temperature regions, i.e., the ionization region from 79 to 170 K, the extrinsic region from ∼170 to 300 K, and the intrinsic region at ≥300 K. The closeness of the determined electronic band gap and the second optical band gap suggests that the conduction electrons in the intrinsic region originate from a thermal excitation from the defect energy levels to the conduction band, which determines the electronic conductivity. It was also found that at or above room temperature, ionic conduction coexists with electronic conduction with a comparable magnitude at ambient pressure and that the intrinsic conduction mechanism also operates at high pressures. These findings provide us a fundamental understanding of the band structure and conduction mechanism of Li-HEO, which would be indispensable to their applications in new technical areas.

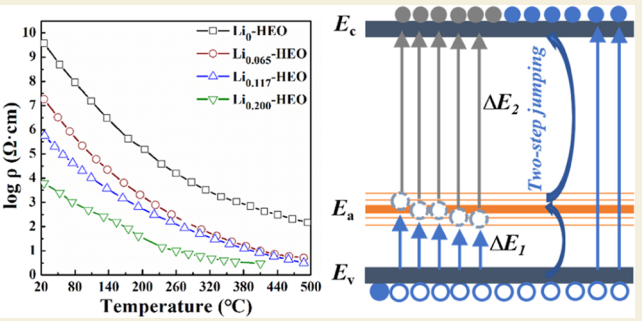

KEYWORDS: *high-entropy oxide, Li doping, p-type semiconductor, electrical conductivity, electrical conduction mechanism, mixed electronic and ionic conduction, high pressure, extreme condition*

1. INTRODUCTION

To cope with global warming and the imminent energy crisis, it is imperative to develop large-capacity and high-efficiency rechargeable batteries and/or supercapacitors in order to store and make efficient use of renewable energies sourced from hydraulic, solar, wind, geothermal, and other sustainable powers.[1−3] For this, researchers are developing high-energy-density electrode/electrolyte materials that are cost-effective and well-functioning, and large capacitor materials that have excellent dielectric properties.[4−8] The emerging high-entropy oxides (HEO)[9] can improve the ionic conductivities of lithium-ion batteries through vacancy formation[10] and lattice distortions.[11] Prior studies showed that the lithium-doped high-entropy oxide $(MgCoNiCuZn)_{1-x}Li_xO$ (denoted Li_x-HEO hereafter) is structurally stable at temperatures up to ∼450 °C and pressures up to ∼50 GPa,[12] and it possesses superionic conductivity and good dielectric properties even at room temperature.[13,14] It was also shown that Li-doped HEO has a reversible conversion and long-term cycling stability during lithiation/delithiation cycles.[15] Thus, Li-doped HEO compounds are new and promising materials for Li-ion batteries and supercapacitors.

Usually, batteries are operated in a mild range of temperatures (e.g., ca. 20−60 °C[16]) and at or near atmospheric pressure. However, in some circumstances, such as for explorations of the deep sea, the South Pole of the earth, and other planets such as Mars, high pressure and/or low temperature may be encountered.[17,18] In other cases, such as in oil and gas explorations, batteries may be exposed to

Received: November 8, 2023
Revised: December 14, 2023
Accepted: January 2, 2024
Published: January 17, 2024

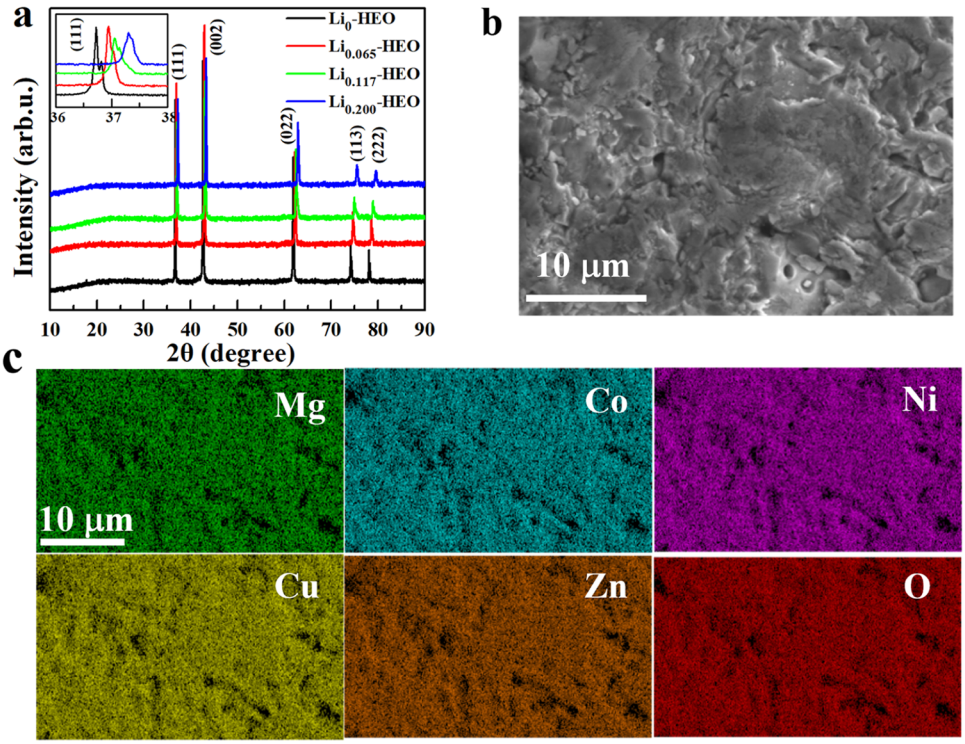

Figure 1. (a) XRD patterns of the synthesized Li_x-HEO samples (x = 0, 0.065, 0.117, and 0.200) at ambient pressure (X-ray wavelength 1.5406 Å). (b) SEM image and (c) EDS elemental mapping of the sample of Li_0-HEO.

temperatures as high as ca. 60−120 °C.[19] Thus, a comprehensive understanding of the structural stability and electrical conduction of the electrode materials (such as Li-doped HEO materials) under extreme conditions is required.

In 2016, Bérardan et al. found that the Li-doped (MgCoNiCuZn)O possesses a colossal dielectric property and a superionic conductivity.[13,14] For instance, at a Li content of x = 0.29, the ionic conductivity of the Li_x-HEO exceeds 10^{-3} S/cm even at room temperature.[14] In 2021, Moździerz et al. found that the Li_x-HEO is a mixed ionic and electronic conductor at room temperature.[20] In these prior works, the electrical conductivities were measured at ambient pressure and at room temperature or in a relatively narrow temperature range (e.g., −40 to 100 °C). Recently, we studied the electrical conductivity of undoped (MgCoNiCuZn)O at pressures up to ∼45 GPa at room temperature.[21] It was found that above ∼22 GPa, the electrical conductivity could be significantly increased by external compression. Nevertheless, there is still a need for an essential understanding of the temperature and pressure dependence of the electrical conductivity of Li-doped (MgCoNiCuZn)O in a wider temperature range and/or at high pressure. In particular, the underlying conduction mechanism under these conditions is still unknown. Thus, in this work, we prepared four Li_x-HEO samples (x = 0, 0.065, 0.117, and 0.200) and studied comprehensively their electrical conductivities in a wide range of temperatures (from 79 up to 773 K) or at high pressures (up to ∼50 GPa). On the basis of the acquired data and analysis, we uncovered the semiconductor band structure and the conduction mechanism of Li_x-HEO, which will have important significance to the design and development of advanced Li-ion batteries that are operable in extreme conditions.

2. EXPERIMENTAL SECTION

A detailed description of the experimental procedures is documented in the Supporting Information. Briefly, four samples of undoped and Li-doped HEO with the nominal formula $(MgCoNiCuZn)_{1-x}Li_xO$ (x = 0, 0.065, 0.117, and 0.200) were synthesized from solid-state reactions at 1000 °C (hereafter, the samples are denoted Li_x-HEO). The samples were characterized by X-ray diffraction (XRD) for the phases and crystal structures, scanning electron microscope (SEM) for morphologies, energy-dispersive X-ray spectroscopy (EDS) for elemental distributions and contents, inductively coupled plasma atomic emission spectrometry (ICP-AES) for Li contents, ultraviolet−visible(−near) infrared (UV−vis−NIR) spectroscopy for optical band gaps, X-ray photoelectron spectroscopy (XPS) for element valence states, electron paramagnetic resonance (EPR) spectroscopy for oxygen vacancy, and thermoelectric open-circuit voltage (OCV) for the carrier type of a semiconductor HEO sample.

The electrical resistance/resistivity of a sample was measured at chosen temperature and pressure values. At room temperature and above, a direct current (DC) Ohmmeter with two probes was used to measure the electrical resistance based on Ohm's law. A DC van der Pauw method[22] with four probes was used to measure the electrical resistivity of a sample loaded in a diamond anvil cell (DAC) at high pressures (see Figures S1 and S2a). The DC methods could only measure the electronic resistance (conductivity) in a material because the movement of ions (e.g., Li^+ ions) into the measuring circuit is prohibited by the sample/probe interface. In order to measure the ionic conductivity, an electrochemical impedance spectroscopy (EIS) was used, which can measure both the ionic and electronic conductivities of a material. At low temperatures (77−300 K), a commercial Hall effect measurement system (HEMS) was used to measure the electrical resistivity (see Figure S2b,c).

Transmission electron microscopy (TEM) was used to observe the microstructures of chosen samples quenched from a high pressure. In situ high-pressure UV−vis spectra (or Raman spectra) of samples in compression and decompression were collected for derivation of the optical band gaps (or for identifying any possible phase changes).

https://doi.org/10.1021/jacsau.3c00693
JACS Au 2024, 4, 592−606

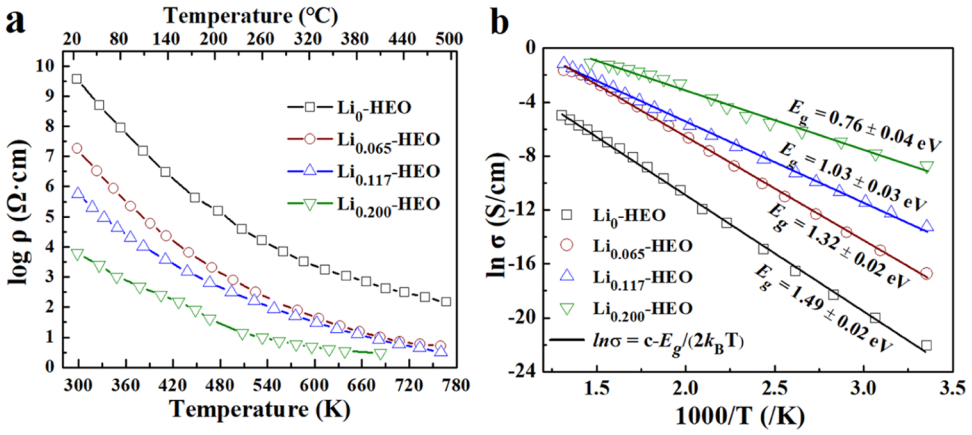

Figure 2. (a) Electrical resistivity of Li_x-HEO as a function of temperature. (b) ln σ of Li_x-HEO as a function of 1000/T. Lines are the fitting curves.

3. RESULTS

3.1. Characterization of Synthesized Samples

The XRD patterns (Figure 1a) of the synthesized Li_x-HEO samples (x = 0, 0.065, 0.117, and 0.200) revealed that they are all in the rock salt structures (space group $Fm\bar{3}m$). The SEM images (Figures 1b and S3) and the EDS elemental mapping (Figures 1c and S3) show that the sample elements are evenly distributed in the sample grains. The total cation contents (Table S1) determined by the EDS analysis are ~10% higher than those given by the chemical stoichiometry calculated from the raw material masses, while the content of oxygen is ~10% less than that given by the chemical stoichiometry (Table S1). These deviations are due to the low accuracy of the EDS in quantitative determinations of concentrations of light elements (e.g., O).[23] However, the contents of each cation by the EDS analysis are close to each other (which would be ~10% according to the calculated stoichiometry). Accordingly, we assume that the cations have equal molar numbers in a sample. With this assumption and based on the principle of mass and charge balances, the nominal formulas of the synthesized samples were derived using the Li content determined by the more accurate ICP-AES (Table S1).

Figure 1a (inset) also reveals that with the increase in the Li content, the XRD (111) peak shifts to a higher 2θ angle. This indicates that there is an increasing contraction of the unit cell, probably due to the increasing content of oxygen vacancies caused by doping of more Li^+ into the HEO cation lattice. The higher the Li content, the more the oxygen vacancy, the higher the lattice strain, and hence the more the lattice contraction. The decrease of the lattice parameter (a) derived from the Rietveld fitting (Figure S4a–d) with the increase of the Li content is shown in Figure S4e, which agrees quite well with the data by Moździerz et al.[20]

3.2. Structural Stability of Li_x-HEO at High Pressures

In our previous work,[12] the structural stability of an undoped and two Li-doped HEO (Li content x = 0.05 and 0.07) were studied. It was found that these compounds are structurally stable (i.e., no phase transitions) at pressures up to ~50 GPa, and at temperatures as high as ~450 °C. On the basis of the prior finding, we infer that the Li_x-HEO compounds synthesized in the present work are also structurally stable at pressures up to ~50 GPa at room temperature. To test this, we used high-pressure Raman spectra (Figure S5) and TEM (Figure S6) to study the structural stabilities of three chosen Li_x-HEO samples (x = 0, 0.065, and 0.117) at high pressure. The results show that at a pressure up to ca. 40–45 GPa, the two characteristic Raman peaks of Li_x-HEO (shown in Figure S5b,d,f) shift almost linearly with the pressure. This indicates that no phase transitions had occurred in the Li-HEO at the high pressure applied.

Selected area electron diffraction (SAED) pattern of the undoped HEO quenched from ~43 GPa (Figure S6a) and that of $Li_{0.065}$-HEO (Figure S6b) quenched from ~22 GPa show that the patterns can all be indexed with a single phase in the $Fm\bar{3}m$ space group. The SAED of $Li_{0.117}$-HEO quenched from ~41 GPa (Figure S6c) exhibits some polycrystalline rings, arising from partial nanosizing at high pressure. However, the SAED rings can still be indexed by the $Fm\bar{3}m$ space group. These SAED and the high-pressure Raman data (Figure S5) show that the Li_x-HEO compounds under study would remain the rock salt structure in our high-pressure electrical conductivity measurements.

3.3. Electrical Conductivity of Li_x-HEO in the Temperature Range of ca. 20–500 °C at Ambient Pressure

The electrical conductivities of the four Li_x-HEO samples (x = 0, 0.065, 0.117, and 0.200) in the temperature range of ca. 20–500 °C were measured in two heating/cooling cycles. The obtained resistivities (Figure S7) are quite consistent irrespective of the cycling number and direction. The data averaged from the two heating stages were documented in Table S2 and illustrated in Figure 2a. It is seen that at room temperature, the resistivity drops nearly 6 orders of magnitude as the Li content increases from x = 0 to 0.200, i.e., from ~3.8 × 10^9 to ~6.2 × 10^3 Ω·cm. From ~20 to 500 °C, the resistivity of the Li_x-HEO samples decreases by about 7, 6, 5, and 3 orders of magnitude, respectively, for the Li content of x = 0, 0.065, 0.117, and 0.200 (Figure 2a). It is noteworthy that the resistivities of the Li-doped samples (x > 0) drop to become only a few Ohms at the highest temperature of ca. 400–500 °C (Figure 2a and Table S2). All of the data demonstrate the semiconductor behavior of the Li_x-HEO sample and the great effect of lithium doping on improving the electrical conductivity of the (MgCoNiCuZn)O high-entropy oxide.

For a semiconductor with electrons (e) and holes (h) as the charge carriers, its electrical conductivity (σ) is proportional to the sum of their carrier mobilities (u_e + u_h) and the carrier concentration (n_i),[24]

https://doi.org/10.1021/jacsau.3c00693
JACS Au 2024, 4, 592–606

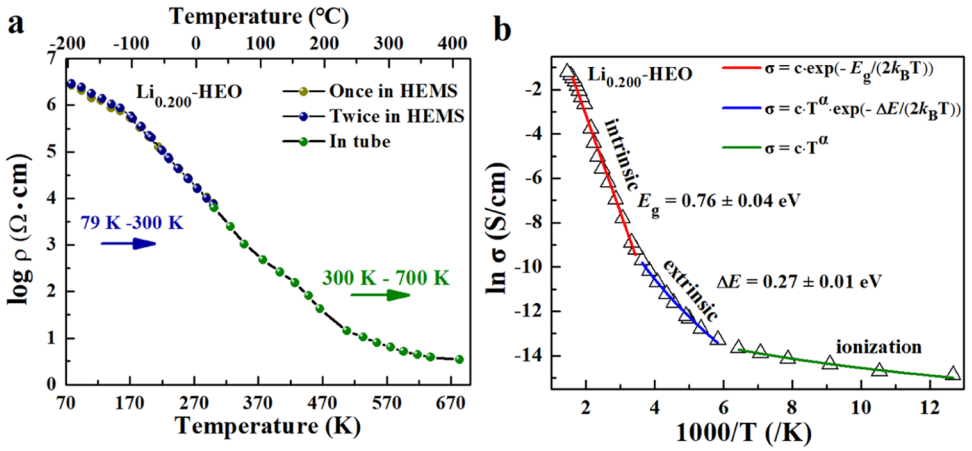

Figure 3. (a) Electrical resistivity as a function of temperature and (b) $\ln \sigma$ as a function of $1000/T$ for the $Li_{0.200}$-HEO sample.

$$\sigma = q_e n_i (u_e + u_h) \tag{1}$$

where q_e is the charge of an electron. The carrier concentration is a function of temperature T and band gap E_g:[25]

$$n_i = c' T^{3/2} e^{(-E_g/2k_BT)} \tag{2}$$

where k_B is the Boltzmann constant and c' is a proportional coefficient. The carrier mobility is governed by lattice scattering and ionized impurity scattering. The former dominates at high temperatures (e.g., tens to hundreds °C), while the latter at low temperatures (e.g., lower than room temperature). According to the first-order scattering theory, the carrier mobility is proportional to $T^{-3/2}$ at high temperatures.[25] With this in consideration and by inserting eq 2 into eq 1, we obtain

$$\sigma = c'' q_e e^{(-E_g/2k_BT)} \tag{3}$$

where c'' is another proportional coefficient. Equation 3 can be written as an Arrhenius equation-like form (with $c = c'' \cdot q_e$)

$$\ln \sigma = \ln c - \frac{E_g}{2k_BT} \tag{4}$$

Using the data in Figure 2a, ln(conductivity) was plotted as a function of $1000/T$ for all of the samples (Figure 2b), which shows a good linear relationship and proves the applicability of eq 4. This indicates that in the temperature range of 20−500 °C, Li_x-HEO behaves as an intrinsic semiconductor, i.e., the electrical conduction is dominated by the electron hopping from the valence band (VB) to the conduction band (CB).[25,26]

The electronic band gaps of the four Li_x-HEO samples were derived from linear regressions based on eq 4. These are, respectively, 1.49, 1.32, 1.03, and 0.76 eV for x = 0, 0.065, 0.117, and 0.200. The decrease of the electronic band gap with the increasing Li content is likely due to the effect of the doping-induced lattice contraction on the band gap and/or the introduction of a middle band consisting of many defect energy levels in the semiconductor electronic band, which allows the electrons in the valence band maximum (VBM) to jump to the conduction band minimum (CBM) using the middle band as the springboard (see below).

3.4. Electrical Conductivity of $Li_{0.200}$-HEO in the Temperature Range of 79−700 K (−194 to 427 °C) at Ambient Pressure

As a representative, the low-temperature resistivity of the $Li_{0.200}$-HEO sample was measured from 79 to 300 K using a HEMS (Figures 3a and S8a,b). Figure 3a shows that the resistivities measured by the commercial HEMS (in 79−300 K) and those measured in a lab furnace (the sample in a quartz tube) in ca. 300−700 K (Figure 2a) form a continuous resistivity curve in the whole temperature range of 79−700 K. In this temperature range, the resistivity decreases monotonically with the increasing temperature, showing the semiconductor behavior of the $Li_{0.200}$-HEO sample.

A plot of $\ln \sigma$ vs $1000/T$ of the sample in the whole temperature range reveals three sections with different slopes (Figure 3b). This is in line with the theory on the electrical properties of semiconductors,[25] based on which the variation of the electrical conductivity of $Li_{0.200}$-HEO with the temperature can be divided into three regions with different conducting mechanisms: the low-temperature ionization region from 79 to 170 K; the middle-temperature extrinsic region from ∼170 to 300 K; and the high-temperature intrinsic region above ∼300 K. The following equations pertinent to different conduction mechanisms[24,26] can be used to fit the conductivity data measured at different temperature ranges.

$$\sigma = c e^{(-E_g/2k_BT)} \quad \text{(for the intrinsic region)} \tag{5}$$

$$\sigma = c T^{\alpha} e^{(-\Delta E/2k_BT)} \quad \text{(for the extrinsic region)} \tag{6}$$

$$\sigma = c T^{\alpha} \quad \text{(for the ionization region)} \tag{7}$$

In these equations, σ, E_g, ΔE, α, c, and k_B represent, respectively, the electrical conductivity, electronic band gap, energy difference between the CBM and the defect energy maximum, an exponent number, a proportional coefficient, and the Boltzmann constant. Equation 5 is virtually equivalent to eq 4.

The fittings of the resistivity data to the relevant equation are shown in Figures 3b and S8a−c. The fitting results show that eqs 5−7 can describe the electrical conductivity of $Li_{0.200}$-HEO quite well in the whole temperature range of 79−700 K. Figure S8d shows the variation of the HEMS-measured carrier concentration and mobility as a function of $1/T$ from 79 to 300 K. It is seen that with increasing $1/T$ (decreasing temperature), the carrier concentration decreases, while the

https://doi.org/10.1021/jacsau.3c00693
JACS Au 2024, 4, 592−606

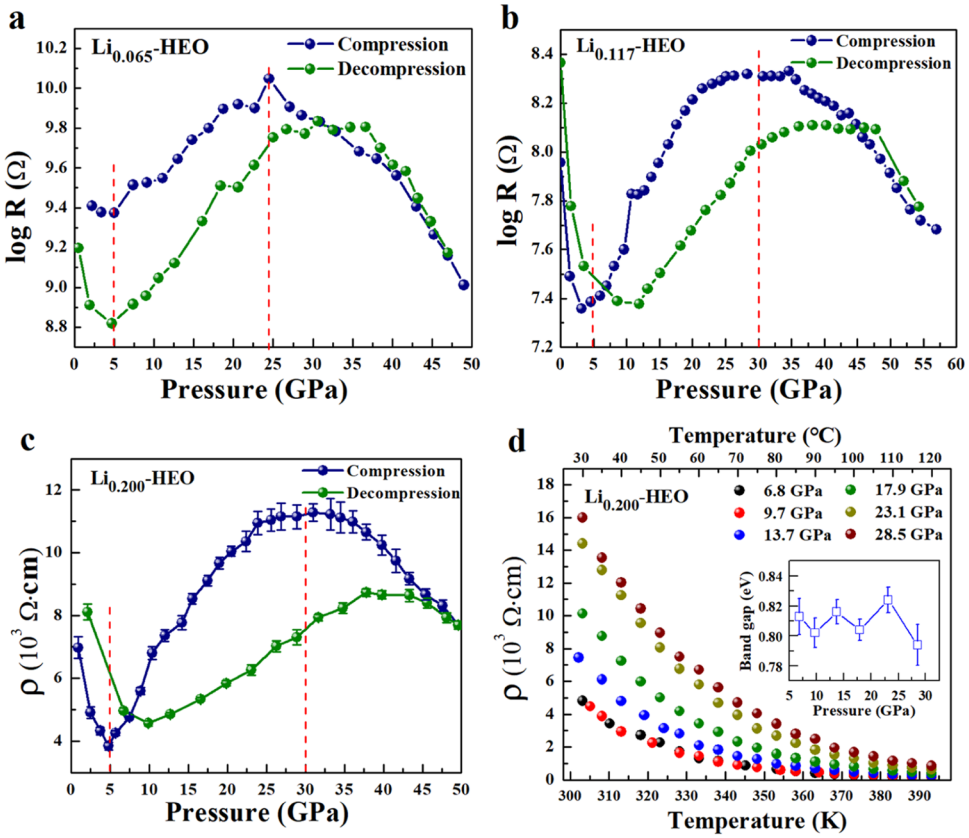

Figure 4. Electrical resistance of $Li_{0.065}$-HEO (a) and $Li_{0.117}$-HEO (b), and resistivity of $Li_{0.200}$-HEO (c) measured at different pressures and at room temperature. Measured resistivity of $Li_{0.200}$-HEO as a function of temperature at given pressures (d). The inset shows the fitting-derived band gaps of $Li_{0.200}$-HEO using Arrhenius-like equation, eq 4.

carrier mobility increases. The shape of the carrier concentration curve (Figure S8d) is similar to that of $ln\sigma$ in Figure 3b in 79−300 K. From the changes of the slopes of the carrier concentration and mobility curves, the low-temperature range can also be divided into the extrinsic and ionization regions (Figure S8d), which are basically consistent with those shown in Figure 3b.

3.5. High-Pressure Electrical Conductivity of Li_x-HEO at Room Temperature or in ca. 30−120 °C

In a prior work, we determined the electrical resistance of an undoped HEO from ∼2 to 43 GPa.[21] It was found that the resistance remains almost unchanged below ∼20 GPa, while it drops markedly above ∼20 GPa. In the present work, the resistances and/or resistivities of the Li_x-HEO compounds (x = 0.065, 0.117, and 0.200) at different pressures were determined (Figure 4a−c). It is seen that for all of the three compounds under compression, the resistance/resistivity decreases from the initial pressure (∼0 GPa) to ∼5 GPa, then increases from ∼5 to ∼25 or 30 GPa, and then decreases from ∼25 or 30 GPa to the highest pressure of ∼50 or 57 GPa. In ca. 0−5 GPa, the quick drop of the resistance/resistivity is likely due to a combined effect of the sample grain compaction,[27] which reduces the grain contact resistance, and the decrease of the band gap due to a lattice contraction that overweighs an electronic repulsion in this pressure range (see Figure 9b), and the nonmonotonic change of the resistance/resistivity with the pressure above ∼5 GPa is likely due to a shift of the pressure dependence of the carrier concentration and/or carrier mobility above ∼25 or 30 GPa.[27] In decompression, the pressure dependence of the resistance/resistivity is basically reversed with respect to that in compression, although they do not fully overlap due to the hysteresis in the structural relaxation.

The resistance of the undoped HEO decreases by ∼3 orders of magnitude upon compression from ∼0 to 43 GPa.[21] By comparison, the resistance/resistivity of the Li_x-HEO (x = 0.065, 0.117, and 0.200) drops only by ∼1 order of magnitude upon compression from ∼0 to 50 GPa (Figure 4a−c). This is likely due to an enhanced carrier concentration due to a decrease in the band gap after Li doping (Figure 2b), which makes the electrical conduction in a Li_x-HEO less sensitive to pressure than that in an undoped HEO.

In order to examine the influence of temperature on the electrical conduction of a Li-doped HEO at a given high pressure, the electrical resistivity of $Li_{0.200}$-HEO was measured using the van der Pauw method at temperatures ranging from ∼30 to 120 °C and the pressure was set to a value in the range of ∼7 to ∼29 GPa (Figure 4d). It is seen that increasing the temperature markedly reduces the resistivity. From linear least-squares fitting of the conductivity data to the Arrhenius-like equation, eq 4 for the intrinsic conduction region, we obtained the electronic band gaps of $Li_{0.200}$-HEO at different pressures (Figure 4d, inset). Results show that the high-pressure electronic band gaps fluctuate around 0.81 eV, which is ∼0.05 eV higher than the electronic band gap of 0.76 eV at ambient pressure (Figure 3b). This indicates that the pressure has a minor suppression effect on generating electron−hole pairs in the $Li_{0.200}$-HEO.

https://doi.org/10.1021/jacsau.3c00693
JACS Au 2024, 4, 592−606

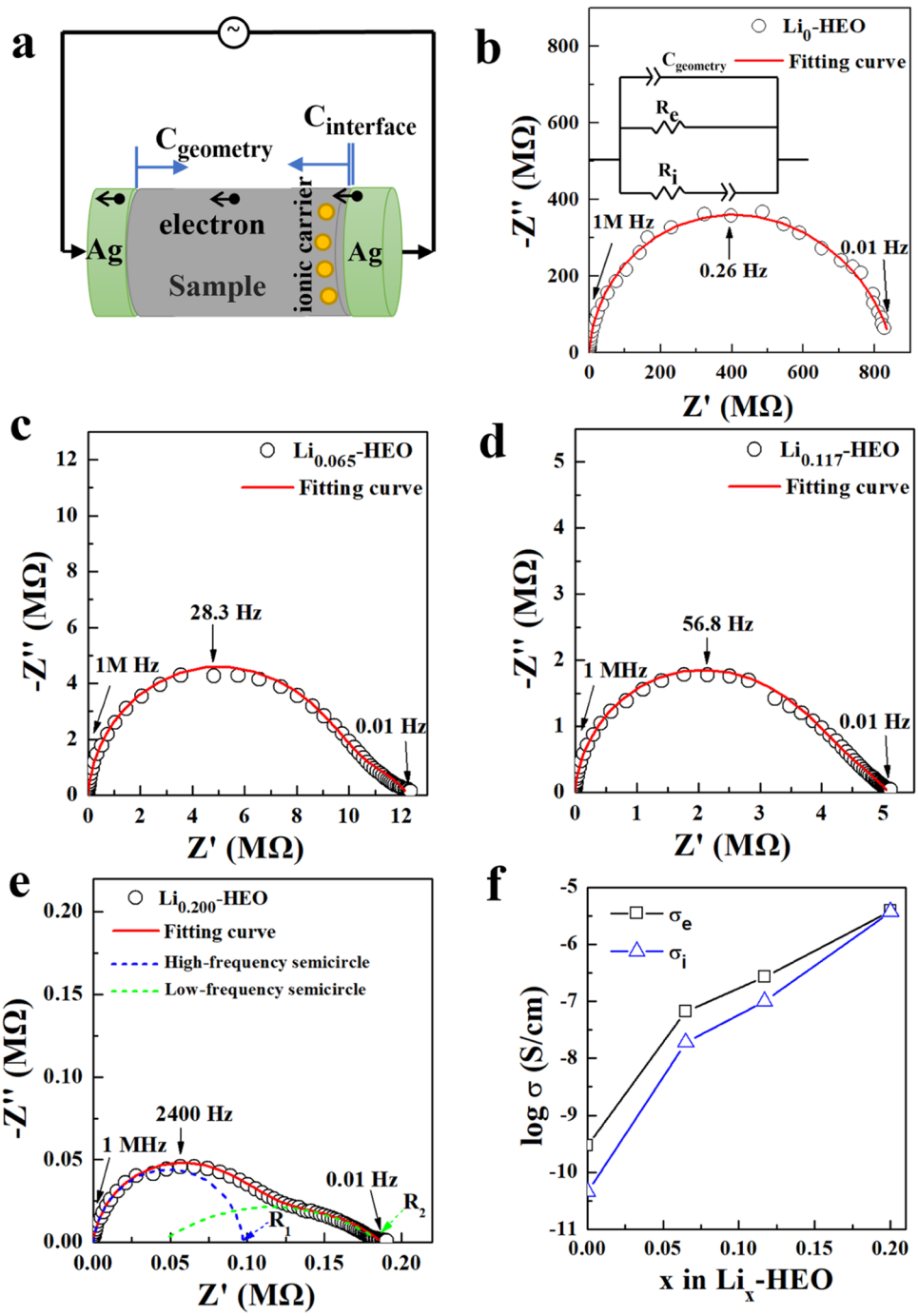

Figure 5. (a) Schematic diagram of the EIS setup. (b)−(e) EIS data (points) and the corresponding fittings (curves) of Li_x-HEO (x = 0, 0.065, 0.117, 0.200) at 23 °C. The inset in (b) is the equivalent circuit. (f) Derived electronic and ionic conductivities of Li_x-HEO at 23 °C. R_1 and R_2 can be used to calculate the electronic and ionic transference numbers, respectively (see the Supporting Information).

3.6. Determining both the Electronic and Ionic Conductivities of Li_x-HEO at Low-to-High Temperatures (−192 to 227 °C) at Ambient Pressure

In all of the DC measurements of the electrical conductivities of the Li_x-HEO (above), ionic conduction is prohibited due to the blockage of the ionic motion at the detecting probe-(electrode)/HEO interfaces. In order to determine both the electronic and ionic conductivities in Li_x-HEO, EIS measurements are needed. EIS is a modern technique widely used to study the ionic conductance in solid electrolyte and electrode materials.[11,14,20,28−34]

Figure 5a,b (inset) shows, respectively, the schematics of the EIS setup and its equivalent circuit used to do the numerical fitting from which both the ionic and electronic conductivities of a mixed electronic/ionic conductor can be deduced.[20,29,34] Typically, Ag[33−35] or Au electrodes[20] are used as the ion-blocking electrodes in the EIS measurements. To examine the influence of different ion-blocking electrodes, we conducted a comparative study of the EIS (and the linear sweeping voltammetry (LSV)) measurements of $Li_{0.117}$-HEO using either Ag paste or Au thin films as the ion-blocking electrodes. The EIS results (Figure S9a) show that the derived electronic

https://doi.org/10.1021/jacsau.3c00693
JACS Au 2024, 4, 592−606

and ionic resistances (transference numbers) are quite close when using either the Ag or Au ion-blocking electrodes. The EIS-derived electronic resistances are also consistent with those derived from the DC LSV measurements (Figure S9b). These indicate that EIS can effectively separate the ionic and electronic resistances and that the Ag and Au ion-blocking electrodes function equivalently. Thus, in our subsequent EIS measurements, we used Ag pastes as the ion-blocking electrodes due to their easier preparations.

Figure 5b–e shows that the EIS of the four Li_x-HEO samples (x = 0, 0.065, 0.117, 0.200) consists of two superimposed semicircles, indicating that all of the samples are mixed electronic and ionic conductors (see the Supporting Information for details). With the increase of the Li content (Figure 5b–e), the low-frequency semicircle in the EIS becomes more apparent, indicating an increase in the ionic conductivity. From the data fitting (Figure 5b–e), the electronic and ionic conductivities of the four Li_x-HEO samples were obtained (Table S3 and Figure 5f). The electronic and ionic transference numbers (t_e and t_i) were also derived (Table S4). These results show that the electronic conduction predominates in Li_0-HEO (t_e = 0.87). However, with the increase of the Li dopant content, the ionic conduction increases (t_i increases) and it is nearly equal to the electronic one in the x = 0.200 sample (t_i = 0.49).

Figure S10 shows the EIS of $Li_{0.065}$-HEO while ascending/descending the temperatures in two heating/cooling cycles (25–227 °C). These diagrams show that with increasing temperature both the real and imaginary parts of the impedance are decreasing, as revealed by the shrinking of the two impedance semicircles. This indicates the increase in the electronic/ionic conductivity with the increasing temperature. Figure S11 shows the EIS of $Li_{0.117}$-HEO at low temperatures (23 to −192 °C). As the temperature decreases, both the high- and low-frequency semicircles enlarge, indicating a decrease of the electronic/ionic conductivity with decreasing temperature. Moreover, the low-frequency semicircle tends to merge into the high-frequency semicircle (which is more apparent in Figure S11f), indicating the ionic conductivity decreases more than the electronic one. At −192 °C, only half of the high-frequency semicircle exists (Figure S11g). This indicates that the conduction is almost fully contributed by the electronic one (the ionic one is negligible).

Using the equivalent circuit (Figure 5b), the EIS spectra of $Li_{0.065}$-HEO and $Li_{0.117}$-HEO were fitted (Figures S10 and S11), and their electronic and ionic conductivities were obtained (Tables S5 and S6 and Figure 6). For $Li_{0.065}$-HEO, in the heating stage of the first heating/cooling cycle, the electronic conductivity predominates over the ionic one below ~89 °C (Figure 6a), while in the second heating stage (Figure 6b), it predominates over the ionic one in the whole temperature range (ca. 20–210 °C). The data from the second heating stage were considered more reliable because after the structural relaxation in the first heating/cooling cycle, both the crystal structure and the electrical conductivity of the sample would be more stabilized. According to the equation $\ln \sigma = \ln A - \frac{E_a}{k_B T}$[36] (where A is a pre-exponential constant, k_B is the Boltzmann constant, and E_a is the activation energy), the activation energies for the electronic and ionic conduction of $Li_{0.065}$-HEO could be derived from the data fitting, which are, respectively, 0.64 and 0.71 eV. Due to the closeness of the activation energies, the temperature dependences of the electronic and ionic conduction are similar, and their magnitudes are also comparable.

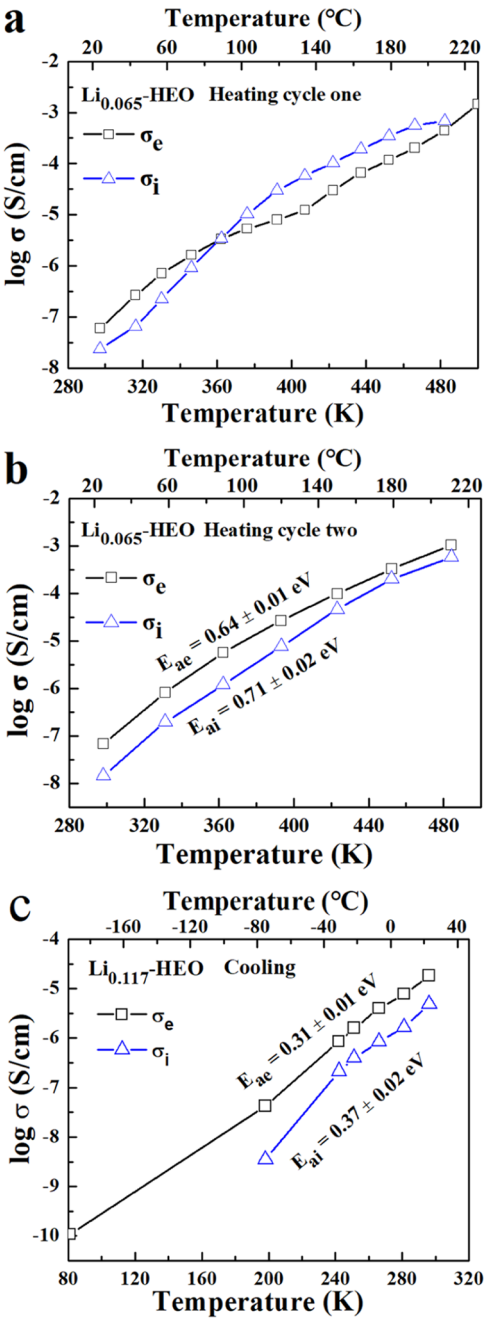

Figure 6. Electronic and ionic conductivities of $Li_{0.065}$-HEO at the first (a) and second (b) heating cycles; (c) electronic and ionic conductivities of $Li_{0.117}$-HEO at low temperatures.

For $Li_{0.117}$-HEO at low temperatures, both the electronic and ionic conductivities decrease with the decreasing temperature (Figure 6c). The derived activation energies of the electronic and ionic conduction are, respectively, 0.31 and 0.37 eV. This explains the faster decrease of the ionic conductivity than the electronic one, as inferred from the evolution of the EIS semicircles with temperature (above).

3.7. Pressure Dependence and Activation Volume of the Ionic Conductivity of $Li_{0.065}$-HEO at Room Temperature

Figures 7 and S12 show the EIS spectra of $Li_{0.065}$-HEO at pressures from 1.5 to 10.0 GPa. The shapes of the EIS curves

https://doi.org/10.1021/jacsau.3c00693
JACS Au 2024, 4, 592–606

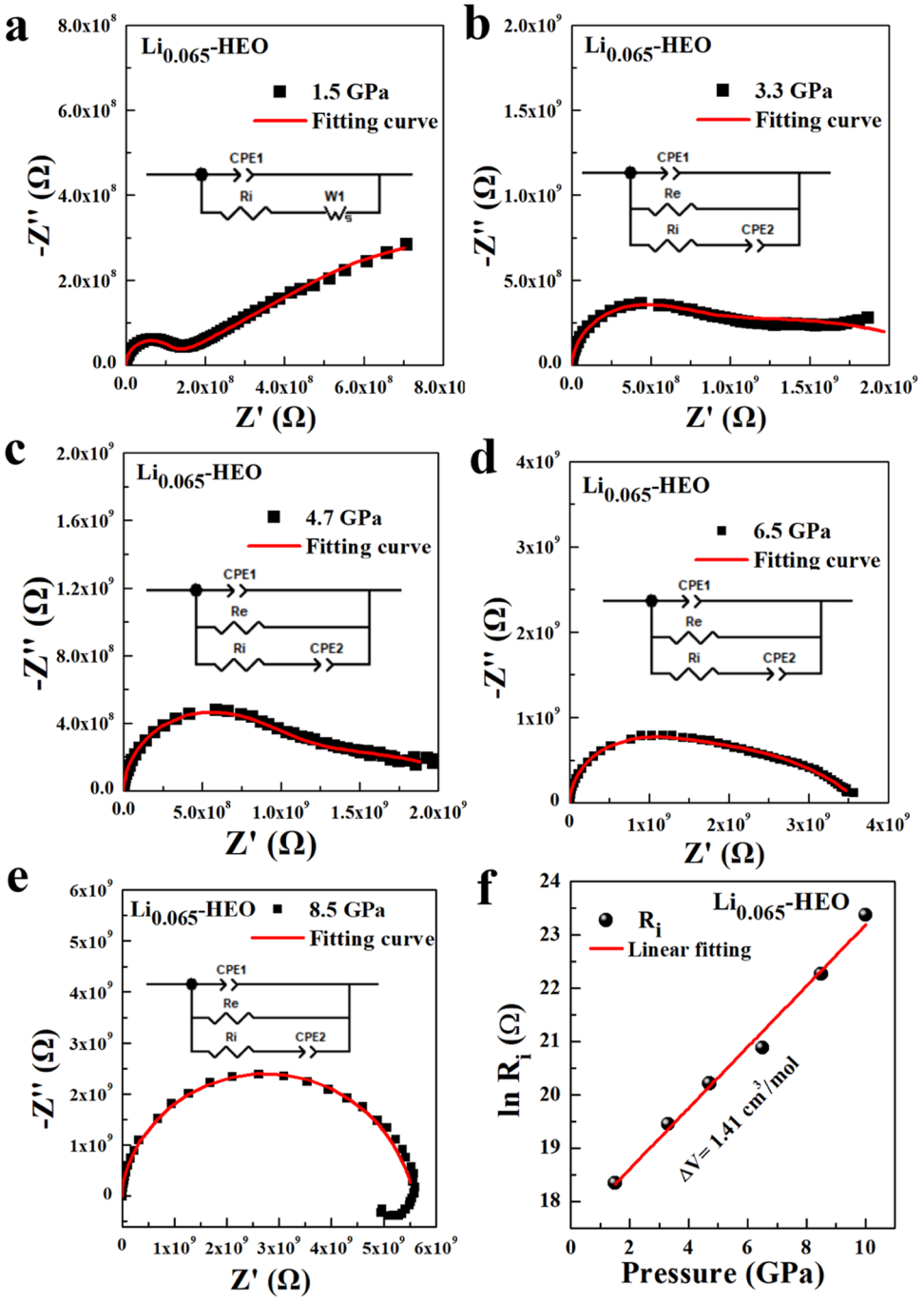

Figure 7. (a–e) EIS (points) and the corresponding fitting (curves) of $Li_{0.065}$-HEO at (a) 1.5 GPa, (b) 3.3 GPa, (c) 4.7 GPa, (d) 6.5 GPa, and (e) 8.5 GPa. The insets in (a–e) are the equivalent circuits. (f) Ionic resistance as a function of pressure.

reveal the variation of the ionic/electronic conduction with the pressure (see the Supporting Information). At 1.5 GPa (Figure 7a), the conduction is dominated by the ionic one since the EIS exhibits a high-frequency semicircle with a low-frequency upward-tipped tail. As the pressure increases (Figure 7b–d), the low-frequency semicircle appears and becomes more apparent, indicating the gradual suppression of the ionic conduction and enhancement of the electronic one. At 8.5 and 10.0 GPa (Figures 7e and S12), an inductive semicircle appears in the EIS (which has negative ordinate values), which can be attributed to the lattice stretching due to the electrostriction effect, as seen in $CaZrO_3$,[37] $LiTaO_3$,[38] and $LiNiO_3$.[38] From the fitting of the EIS data (Figures 7a–e and S12) using the equivalent circuits (Figure 7a–e, insets; the inductive semicircles in Figures 7e and S12 were not fitted), the ionic conduction resistance (R_i) was obtained as a function of the pressure (Figure 7f). Using the data in Figure 7f, the activation volume (ΔV) of the ionic conduction can be derived from the following equation[39] (see the Supporting Information for derivation).

$$\Delta V = -k_B T \frac{\partial \ln R_i}{\partial P} \tag{8}$$

where R_i is the ionic resistance and P is the pressure. Physically, ΔV may be interpreted as the volume change for ionic migration, and it is a measure of the potential barrier for

https://doi.org/10.1021/jacsau.3c00693
JACS Au 2024, 4, 592–606

migration of the conducting ions through the crystal lattice.[40,41]

Figure 7f shows that the logarithm of the ionic resistance of $Li_{0.065}$-HEO exhibits a linear relationship with the pressure at room temperature (23 °C). Thus, using the slope of the linear regression equation between ln R_i and P, we obtained the ionic activation volume of 1.14 cm^3/mol according to eq 8.

In Table S7, we compared the ionic activation volume of $Li_{0.065}$-HEO to reported values of some other ionic conductors. Its magnitude is comparable to those of several fast ionic conductors such as $La_{0.52}Li_{0.35}TiO_{2.96}$ (1.6−1.7 cm^3/mol).[42] Accordingly, $Li_{0.065}$-HEO can be classified as a fast ionic conductor even at room temperature due to its relatively small migration barrier (ΔV).

3.8. Optical Band Gaps of Li_x-HEO at Ambient Pressure and Room Temperature

The electronic band gap of Li_x-HEO obtained from the electrical conductivity measurements (above) is the threshold energy of creating unbound electron−hole pairs in the semiconductor under the polarization of an external electric field. On the other hand, the optical band gap obtained from UV−vis−NIR measurements is the threshold energy for exciting the electrons from the VBM (or from a middle band) to the CBM (or to a middle band) by adsorption of the supplied photons. The derived optical band gaps may provide more details about the semiconductor band structure, such as whether a middle band is formed by enclosing defect energy levels.

Figure 8a shows the measured UV−vis−NIR spectra of Li_x-HEO at ambient pressure. It is seen that two apparent absorption humps (peaked at ∼800 and 1250 nm, respectively) are present in the undoped HEO (x = 0), while the absorption humps of the doped Li_x-HEO (x > 0) are broadening and their intensities are increasing with increasing Li content. This suggests that more and more defect energy levels are present in the Li-doped HEO electronic band, which tend to smear out the adsorption humps.

Figure 8b,c shows the Tauc−Mott plots of the UV−vis−NIR data in the direct (Figures 8b and S13a,b) or indirect (Figure 8c) band gap mode for the light adsorption.[27,43] In these plots, A is the absorbance of the light by a sample and E is the photon energy. Figure 8b shows that when a Li_x-HEO is treated as a direct band gap semiconductor, three band gaps can be identified in the experimental photon energy range for all four Li_x-HEO samples. These are optical band-I gap: ca. 0.4−0.5 eV, optical band-II gap: ca. 1.1−1.2 eV, and optical band-III gap: ca. 1.7−1.8 eV. Moreover, the band gap usually decreases with an increasing Li content. Nonetheless, in the indirect band gap plot (Figure 8c), only optical band-II and band-III gaps could be derived because too far extrapolations would have to be conducted in order to get the band-I gaps, which make them unreliable.

It is noted that there are a few minor dents in the UV−vis−NIR curves due to changes of the light source (Figure 8a), which were also observed in those of some reference semiconductors (Si, NiO, CuO, and ZnO; see Figure S13). However, these do not affect the correct determinations of the band gaps of the materials under study, as shown in Figure S13 and Table S8.

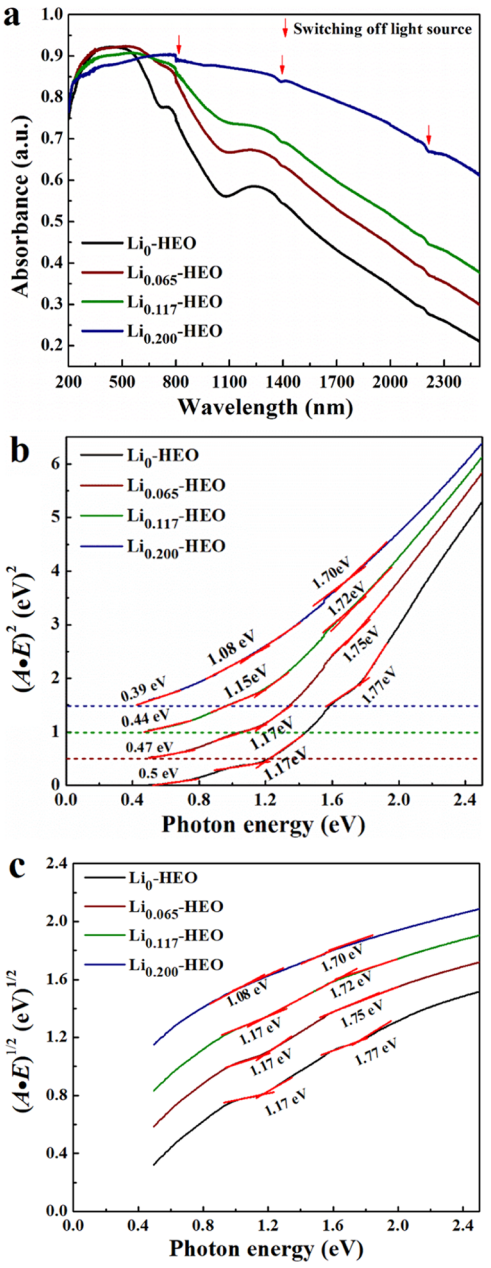

Figure 8. UV−vis−NIR absorption spectra (a), plot of $(A{\cdot}E)^2$ as a function of E (b), and plot of $(A{\cdot}E)^{1/2}$ as a function of E (c) of Li_x-HEO (x = 0, 0.065, 0.117, and 0.200). For clarity, in (b) and (c), the curves for x > 0 were sequentially shifted upward by 0.5 and 0.2 units, respectively.

3.9. Optical Band Gaps of $Li_{0.065}$-HEO at High Pressures and Room Temperature

The high-pressure UV−vis absorption spectra of $Li_{0.065}$-HEO in compression and decompression were measured (Figure S14a,b). The spectra at three chosen pressures (4.4, 28.2, and 50.1 GPa) are shown in Figure 9a. Using the Tauc−Mott plots used while treating $Li_{0.065}$-HEO as a direct band semiconductor (Figure S14c,d), the optical band gaps at different pressures were derived (Figure 9b). Note that, in the UV−vis photon energy range, only one optical band gap was obtained due to the narrowed energy range compared to the UV−vis−NIR (above), which is the optical band-III gap (see Figure 8b) as revealed by the UV−vis−NIR data.

https://doi.org/10.1021/jacsau.3c00693
JACS Au 2024, 4, 592−606

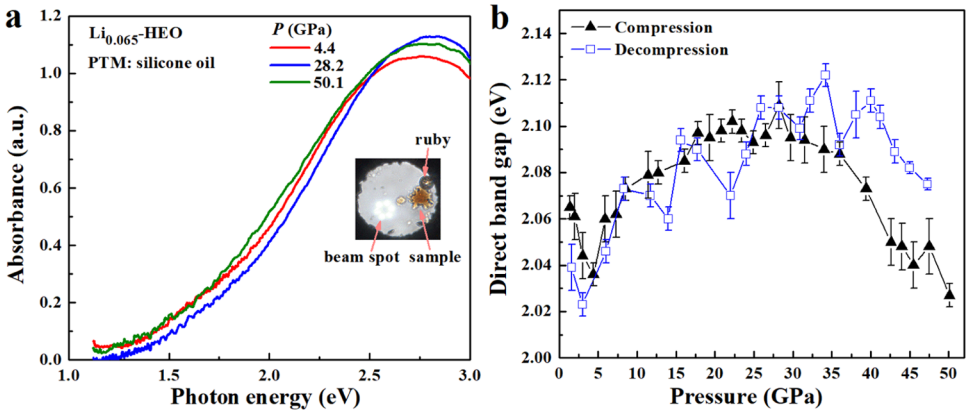

Figure 9. (a) In situ high-pressure UV−vis absorbance spectra of $Li_{0.065}$-HEO at chosen pressures (silicone oil used as the PTM). (b) Variation of the optical band gap as a function of pressure.

The variation of the direct band gap of $Li_{0.065}$-HEO with pressure exhibits a maximum at ∼23 GPa in compression (Figure 9b), similar to the variation of the electrical resistivity with pressure shown in Figure 4a. The increase of the band gap with pressure below ∼23 GPa is likely due to the increased electron repulsion at closer ionic distances, while the decrease of the band gap with pressure above ∼23 GPa is likely due to the band approaching from VBM to CBM at closer ionic distances.

4. DISCUSSION

4.1. Electrical Conduction Mechanism and Band Structure of Li_x-HEO at Different Temperature Ranges at Ambient Pressure

In order to depict the electronic band structure of the Li_x-HEO materials, first we needed to determine the dominant carrier type. We tried to determine the carrier type of the Li_x-HEO samples using the Hall effect measurements (see the Supporting Information). However, due to the small Hall voltages of the HEO ceramic materials, the determined carrier type was less conclusive. Thus, we sought another method, the thermoelectric measurement method, because a negative/positive Seebeck coefficient corresponds to an n-/p-type carrier in the semiconductor.[44,45] Thus, via measuring the sign of the thermoelectric open-circuit voltage, it is possible to determine the carrier type (see the Supporting Information). As a benchmark of this method, the thermoelectric OCV of both an n-type and a p-type silicon were measured, which gives the correct carrier type consistent with the used material (Figure 10a; a positive/negative OCV corresponds to an n-/p-type carrier). Figure 10b shows the OCV of the four Li_x-HEO samples, which reveals that all of the Li_x-HEO samples are p-type semiconductors.

Then, we tried to verify the presence of oxygen vacancies in the samples using both XPS and EPR techniques. The presence of defects such as oxygen vacancy that can lead to the defect energy levels is supported by the measured XPS data of Li_x-HEO (Figure S15). Figure S15b−e shows that Mg, Ni, Cu, and Zn were bivalent, while Co had mixed valences of +2 and +3, as revealed by the XPS curve fitting (Figure S15g,h). The formation of Co^{3+} in the undoped HEO is probably due to the inevitable surface oxidation of Co^{2+} at high temperature,[46] while that in the Li_x-HEO is probably due to both the Co^{2+} oxidation[46] and the requirement of charge compensation because of the doping of Li^+ into the bivalent cation sublattice.[35]

The XPS data of Li_x-HEO (Figures S15f and 10c) show that there are two O 1s peaks. Hsieh et al. and Chen et al.[47,48] attributed the low binding energy peak to the O^{2-} ions surrounded by Zn^{2+} ions in their samples. In reference to this, we attribute the 529.5 eV peak in the spectra to lattice oxygen bonded by cations in Li_x-HEO, which is denoted as O_L in Figure 10c. According to ref 47, the higher binding energy of 531.5 eV is associated with O^{2-} ions that are in an oxygen-deficient environment. Thus, this peak reflects the presence of oxygen vacancies and is denoted as Ov in Figure 10c. Then, the intensity ratio of the O_V to the O_L peaks would scale with the content of the oxygen vacancy. Figure 10d shows that with the increase of the Li content, the amount of oxygen vacancy increases. Even for the undoped HEO, there are still some oxygen vacancies (Figure 10d), which were also observed in prior studies.[46,49] The lattice distortion arising from the cation size mismatch can lead to a significant lattice strain, which may reduce the defect formation energy and promote the generation of metal and oxygen vacancies in the undoped HEO.[46] In the Li-doped HEO, the formation of oxygen vacancies is probably due to both the lattice-distortion origin and the requirement for the charge compensation due to the doping of Li^+ into the bivalent cation sublattice (as for the oxidation of Co^{2+} to Co^{3+}).[35] The presence of the oxygen vacancies in the Li_x-HEO samples was further verified by the EPR data (Figure 10e) because the EPR response at a *g*-factor value of ∼2.01 mainly stems from the unpaired electrons of oxygen vacancies.[46]

On the basis of the above experimental results on the carrier type, defect formation, and optical band gaps, we proposed a temperature-dependent band structure of Li_x-HEO (Figure 10f) to explain the three experimentally deduced electrical conduction mechanisms of Li_x-HEO (x = 0.200; Figure 3b) at different temperature ranges at ambient pressure.

In the low-temperature range (e.g., 79−170 K in Figure 3a), the ionization region dominates (Figure 3b). The thermal energy is not high enough to excite the electrons to hop from the VBM to the CBM. However, due to the Li doping and the presence of oxygen vacancies in the HEO, some defect energy levels form a middle band in the vicinity of the VB and the thermal energy may suffice to excite some electrons from the VBM to the defect energy levels, creating holes as the dominant carrier (i.e., p-type) for electrical conduction (Figure

https://doi.org/10.1021/jacsau.3c00693
JACS Au 2024, 4, 592−606

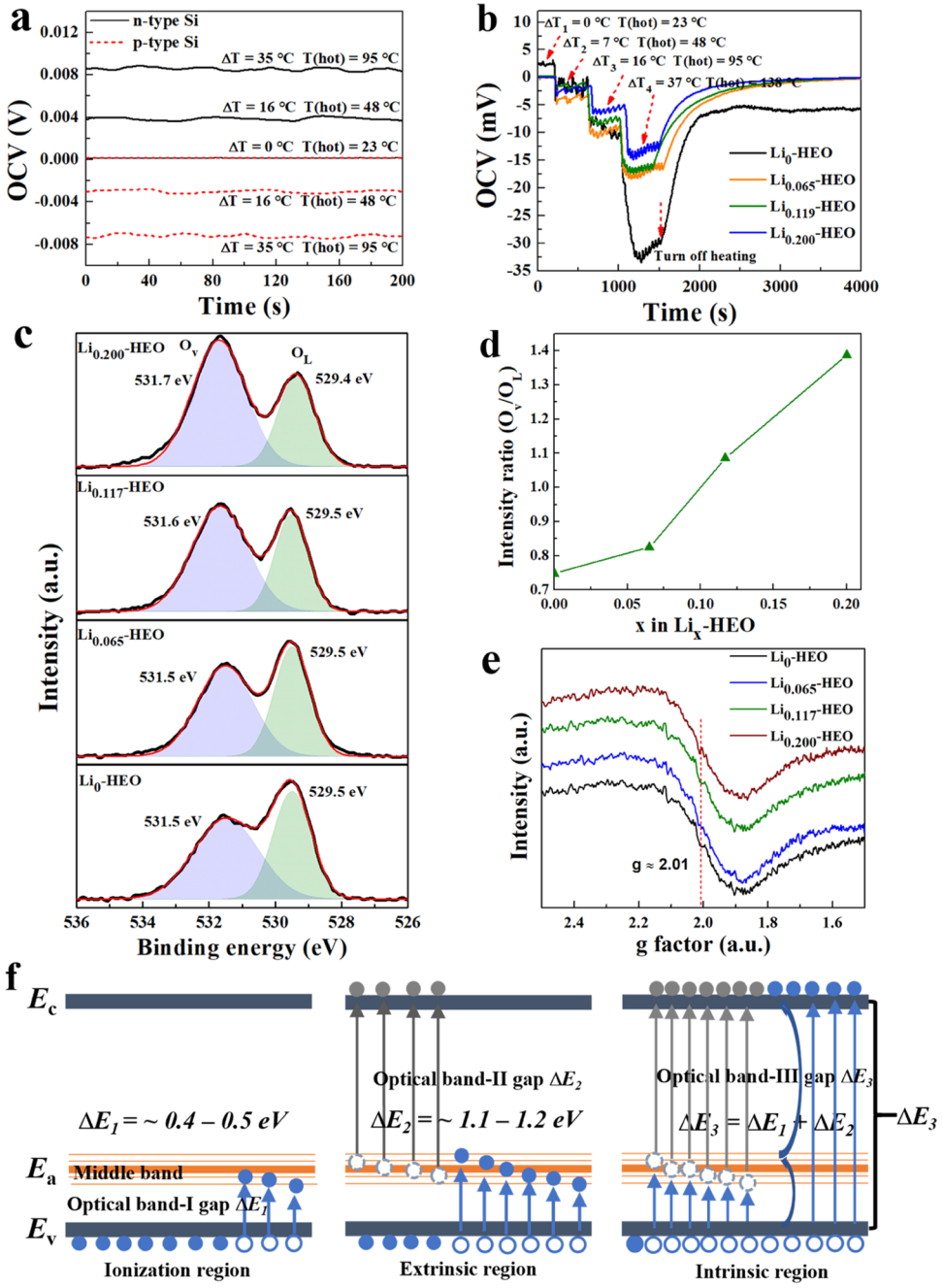

Figure 10. (a) Thermoelectric OCV of a benchmark n- and p-type silicon. (b) Thermoelectric OCV of the Li_x-HEO samples. (c) Measured XPS of oxygen (black curves) in Li_x-HEO and the corresponding fitting (red curves). (d) Intensity ratio of O_v to O_L as a function of x in Li_x-HEO. (e) Electron paramagnetic resonance (EPR) spectra of the L_x-HEO samples. (f) Schematic illustration of ionization, extrinsic, and intrinsic thermal excitations of electrons in Li_x-HEO. Blue solid circles: electrons at the VBM, which may be excited to the defect energy levels or the CBM; blue hollow circles: holes at the VB created by exciting the VBM electrons; gray solid circles: electrons excited from the defect energy levels; gray dashed hollow circles: holes created by exciting the electrons in the defect energy levels.

10f, left). In this region, even though the carrier concentration is low, the carrier mobility is relatively high due to the reduced lattice scattering at low temperatures (Figure S8d). With increasing temperature, the carrier concentration increases, while the carrier mobility decreases (Figure S8d). Overall, the low carrier concentration and the high mobility still create some low electrical conductivity.

In a middle-temperature range (e.g., ca. 170−300 K in Figure 3a), the extrinsic region dominates (Figure 3b). The thermal energy is able to excite many electrons in the VBM to the defect energy levels (forming the dominant charge carrier - holes in the VB). Minor amounts of electrons can also be excited from the defect energy levels to the CBM, leaving some holes in the middle band. However, the VBM electrons are unable to be excited directly to the CBM (Figure 10f, middle). With an increase in the temperature, the carrier concentration increases, yet the mobility remains essentially constant (Figure S8d). The conductivity-derived ΔE of ∼0.27 eV (Figure 3b) and the optical band-I gap of ca. 0.4−0.5 eV (Figure 8b) would correspond to the energy difference (ΔE_1) between the defect

https://doi.org/10.1021/jacsau.3c00693
JACS Au 2024, 4, 592−606

energy levels and the VBM, and the optical band-II gap of ca. 1.1−1.2 eV (Figure 8b,c) would correspond to the energy difference (ΔE_2) between the CBM and the defect energy levels.

In a high-temperature range (>∼300 K in Figure 3a), the intrinsic region dominates (Figure 3b). The thermal energy is high enough to excite most electrons in the defect energy levels to the CBM, which can be supplied by exciting the VBM electrons, and to excite some electrons from the VBM directly to the CBM (Figure 10f, right). These processes also create holes in the VB or the middle band. The conductivity-derived electronic band gap of ca. 0.8−1.5 eV (Figure 2b) is close in magnitude to the optical band-II gap of ca. 1.1−1.2 eV (Figure 8b,c). Thus, both of them correspond to the energy difference (ΔE_2) between the CBM and defect energy levels (Figure 10f). The optical band-III gap of ca. 1.7−1.8 eV (Figure 8b,c) would correspond to the energy difference (ΔE_3) between the CBM and VBM (Figure 10a, right), which should equal to the sum of the optical band-I gap and the band-II gap (i.e., $\Delta E_3 = \Delta E_1 + \Delta E_2$).

The closeness of the electronic band gap (E_g) to the optical band-II gap (ΔE_2) suggests that in the intrinsic region, the electronic conduction is dominated by the electron excitation from the defect energy levels to the CBM rather than the direct electron excitation from the VBM to the CBM. This is reasonable because as long as electrons are readily excited from the VBM to the defect energy levels (with a smaller energy difference of ΔE_1), they are subsequently excited to the CBM (with a bigger energy difference of ΔE_2) for electronic conduction.

Although the electronic band gap (Figure 2b) of Li_x-HEO is close in magnitude to the optical band-II gap (Figure 8b,c), they are not equal. For x = 0 and 0.065, the former is larger than the latter, while for x = 0.117 and 0.200, the former is smaller than the latter. The first case may indicate that the electron−hole binding energy is high enough that some more electrical energy is needed to separate them for producing an actual electrical conduction. The second case may indicate that the electron excitation for the VBM to the defect energy levels (Figure 10f, right) may also contribute to the electrical conduction appreciably, making the overall electronic band gap appear smaller than the optical-II one.

4.2. Electrical Conduction Mechanism of Li_x-HEO at Room Temperature and at High Pressure

As discussed above, above room temperature and at ambient pressure, the electrical conduction of Li_x-HEO is mainly governed by the intrinsic conduction (Figure 3b and Figure 10f, right). At room temperature and high pressure, this conduction mechanism should still operate. This is supported by the fact that the measured high-pressure optical band gap (around ca. 2.02−2.12 eV in Figure 9b) has a magnitude comparable to the optical band-III gap measured at ambient pressure (∼1.8 eV in Figure 8b,c). The good correlation between the trend of the direct band gap vs pressure (Figure 9b) and that of the log(resistance) vs pressure (Figure 4a) suggests the applicability of eq 4, which also supports the conduction is in the intrinsic region.

Without a phase change, the pressure can produce at least two effects on the band gap of a Li_x-HEO semiconductor. With increasing the pressure and hence a closer interaction of the electron clouds, the electron repulsion increases, which may increase the band gap. On the other hand, with the shortening of the atomic bonds at high pressure, the ionic distances are reduced, which may decrease the band gap. The predominance of one effect over the other may produce a nonmonotonic variation of the band gap with pressure, as observed in Figure 9b. This explains the slight difference between the ambient optical band-III gap (Figure 8b,c) and the high-pressure band gap (Figure 9b).

4.3. Ionic Conduction Mechanism of Li_x-HEO at Room Temperature and at High Pressures

Bérardan et al. reported that Li_x-HEO possesses a colossal dielectric property at room temperature.[13] In another work, they concluded that Li_x-HEO is a pure superionic conductor at room temperature.[14] However, their EIS data (their figures 1 and 3) do not show pure ionic feature of EIS[29] (a high-frequency semicircle plus an upward-tipped tail, see the Supporting Information). In fact, their data show more features of a pure electronic conductor (one semicircle in the whole frequency range) or a mixed electronic and ionic conductor (two superimposing semicircles). Our data (Figure 6) clearly show that the Li_x-HEO is a mixed electronic and ionic conductor in a wide range of temperatures.

Although our EIS measurements cannot tell independently the actual carrier for ion migration, numerous previous works showed that Li^+ is the major ionic carrier in lithium superionic conductors (such as $Li_{10}GeP_2S_{12}$,[50] $LiGa(SeO_3)_2$,[51] LiAlSO,[52] and $Li_{1.3}Al_{0.3}Ti_{1.7}(PO_4)_3$[53]), lithium fast ionic conductors (such as $Li_7La_3Zr_2O_{12}$[54] and $Li_6ALa_2Ta_2O_{12}$ (A = Sr, Ba)[55]), and other mixed electronic-ionic conductors (such as $LiCoO_2$,[56] $Li_{0.34}La_{0.55}MO_{3-\delta}$ (M = Ti, Cr, Mn, Fe, Co),[57] $Li_{0.35}La_{0.52}TiO_{2.96}$,[58] and $LiFe_{0.95}M_{0.05}PO_4$ (M = Mg, Ni)[59]). Results from molecular dynamics simulations also showed that Li^+ has a higher self-diffusion coefficient than O^{2-} in $Li_2O_{0.96}$ and $Li_{1.9}O$, and that if no vacancies are generated, there is no significant atomic self-diffusion for ionic migration.[60] Thus, it is expected that Li^+ ions play an important role in the ionic transport in Li_x-HEO due to its higher mobility compared to other ions. On the other hand, O^{2-} may also contribute to the ionic transport, as found in some complex oxides, such as $La_{0.4}Pr_{0.4}Sr_{0.2}In_{0.8}Mg_{0.2}O_{2.8}$ in 160−225 °C.[29] Moreover, the presence of oxygen vacancies in Li_x-HEO should make Li^+ and/or O^{2-} migrate easily through the crystal lattice. Pressure has a suppression effect on the ionic conductivity of Li_x-HEO (Figure 7f), which may be due to the reduction of the ionic migration space due to the lattice shrinkage under compression. Nevertheless, Li_x-HEO has a small activation volume (1.41 cm^3/mol), making it a fast ionic conductor even at pressure up to ∼10 GPa.

5. CONCLUSIONS

Understanding the conduction mechanism at different temperature and pressure conditions is of ultimate importance for developing novel applications of Li-doped high-entropy materials. In this work, we synthesized four $(MgCoNiCuZn)_{1-x}Li_xO$ high-entropy oxide samples (Li_x-HEO, where x = 0, 0.065, 0.117, and 0.200) using high-temperature solid-state reactions. The electrical conductivities of chosen Li_x-HEO samples were measured at temperatures within 79 and 773 K, and/or at pressures from ambient up to ∼50 GPa. It was found that in the temperature range studied, the Li_x-HEO behaves as a semiconductor (p-type in the vicinity of room temperature). Due to the existence of the oxygen vacancy in the Li_x-HEO, defect energy levels are present in the

https://doi.org/10.1021/jacsau.3c00693
JACS Au 2024, 4, 592−606

semiconductor band, forming a middle band that has an important impact on the electrical conductivity. Arrhenius-like plots of the conductivity data (at ambient pressure) revealed that in different temperature regions, different electronic conduction mechanisms operate. In a low-temperature region (79−170 K), ionization conduction dominates, where the relatively low electrical conduction is controlled by the weak thermal excitations of the electrons in the valence band to the defect energy levels. The excitation energy has a magnitude of ca. 0.4−0.5 eV, as estimated from the optical band-I gap. In a middle-temperature region (ca. 170−300 K), the extrinsic conduction dominates, where the rising electrical conduction is controlled by the thermal excitations of small amounts of the electrons in the defect energy levels to the conduction band. The excitation energy has a magnitude of ca. 1.1−1.2 eV, as estimated from the optical band-II gap. In a high-temperature region (>300 K), intrinsic conduction dominates, where the markedly increased electrical conduction is controlled by the increased thermal excitations of the electrons in the semiconductor valence band to the conduction band via the springboard of the defect energy levels, as revealed by the nearly equal electronic band gap (ca. 0.8−1.5 eV) and optical band-II gap (ca. 1.1−1.2 eV).

At (or above) room temperature and high pressures (up to ∼50 GPa), the intrinsic conduction mechanism still operates. However, pressure exhibits a nonmonotonic effect on the electrical conduction, akin to its effect on the optical band gap (and hence the carrier concentration). This is likely due to the trade-off between the pressure-enhanced electron repulsion (which increases the band gap) and the band approaching (which decreases the band gap) at closer ionic distances.

In addition to the electronic conduction, Li ionic conduction also exists in the Li-doped HEO. At room temperature, the ionic conductivity of Li_x-HEO increases with an increasing lithium content. At ca. 20−200 °C, $Li_{0.065}$-HEO has an ionic activation energy of ∼0.7 eV, and at low temperatures, $Li_{0.117}$-HEO has an activation energy of ∼0.4 eV. Meanwhile, pressure has a suppression effect on the ionic conductivity, as revealed by a small ionic activation volume of 1.41 cm^3/mol ($Li_{0.065}$-HEO), which makes the Li_x-HEO a fast ionic conductor.

Our work presented a comprehensive study of the electrical conduction of Li-doped high-entropy oxides $(MgCoNiCuZn)_{1-x}Li_xO$ at different temperature and pressure conditions. The semiconductor band structure was revealed, and the conduction mechanisms were uncovered. This work provides us with fundamental knowledge for developing new generations of HEO-based Li-ion electrode materials that would function in both ambient and extreme conditions.

■ ASSOCIATED CONTENT

Supporting Information

The Supporting Information is available free of charge at https://pubs.acs.org/doi/10.1021/jacsau.3c00693.

Complete experimental details; supplementary figures: photos of samples loaded in DACs, four-probe configuration adopted by the commercial HEMS, SEM and EDS elemental mapping images, Rietveld fitting of XRD patterns, high-pressure Raman spectra, TEM images of samples quenched from high pressure, resistivities from room temperature to 500 °C measured in two heating−cooling cycles, nonlinear least-squares fitting of the conductivity vs temperature of $Li_{0.200}$-HEO from 79 to 700 K, variations of the carrier concentration and mobility of $Li_{0.200}$-HEO as a function of $1000/T$ in the temperature range of 79−300 K, comparison between EIS/LSV results when using either Ag or Au ion-blocking electrodes, EIS spectra of $Li_{0.065}$-HEO in two heating−cooling cycles from 25 to 227 °C, EIS spectra of $Li_{0.117}$-HEO in cooling from 23 to −192 °C, EIS spectra of $Li_{0.065}$-HEO at 10.0 GPa, Tauc plots of the Li_x-HEO samples and several common semiconductors, UV−vis−NIR spectra of Si, NiO, CuO, and ZnO, high-pressure UV−vis absorption spectra and Tauc plots of $Li_{0.065}$-HEO under compression/decompression at up to ∼50 GPa, XPS spectra of the Li_x-HEO samples (x = 0, 0.065, 0.117, and 0.200); supporting tables: elemental contents estimated by EDS analysis and lithium content determined by ICP-AES, resistivity of Li_x-HEO (x = 0, 0.065, 0.117, and 0.200) at different temperatures, capacitance and conductivity of Li_x-HEO (x = 0, 0.065, 0.117, and 0.200) at room temperature derived from fitting of EIS data, resistance and electronic/ionic transference number of Li_x-HEO (x = 0, 0.065, 0.117, and 0.200) at room temperature, capacitance and conductivity of $Li_{0.065}$-HEO derived from fitting of EIS data at high temperatures, capacitance and conductivity of $Li_{0.117}$-HEO derived from fitting of EIS data at low temperatures, activation volumes for ionic conduction of some ionic conductors, and derived optical band gaps of some reference semiconductors (PDF)

■ AUTHOR INFORMATION

Corresponding Author

Hengzhong Zhang − *Center for High Pressure Science and Technology Advanced Research, Shanghai 201203, China;* orcid.org/0000-0003-2322-2274; Phone: +86-21-80177095; Email: hengzhong.zhang@hpstar.ac.cn

Authors

Meng Song − *Center for High Pressure Science and Technology Advanced Research, Shanghai 201203, China*

Xiaoliang Zhang − *Center for High Pressure Science and Technology Advanced Research, Shanghai 201203, China*

Shun Wan − *Center for High Pressure Science and Technology Advanced Research, Shanghai 201203, China*

Gui Wang − *Center for High Pressure Science and Technology Advanced Research, Shanghai 201203, China*

Junxiu Liu − *Center for High Pressure Science and Technology Advanced Research, Shanghai 201203, China;* orcid.org/0009-0007-5949-7735

Weiwei Li − *Center for High Pressure Science and Technology Advanced Research, Shanghai 201203, China*

Hongliang Dong − *Center for High Pressure Science and Technology Advanced Research, Shanghai 201203, China*

Chenjie Lou − *Center for High Pressure Science and Technology Advanced Research, Beijing 100193, China*

Zhiqiang Chen − *Center for High Pressure Science and Technology Advanced Research, Shanghai 201203, China*

Bin Chen − *Center for High Pressure Science and Technology Advanced Research, Shanghai 201203, China*

Complete contact information is available at: https://pubs.acs.org/10.1021/jacsau.3c00693

https://doi.org/10.1021/jacsau.3c00693
JACS Au 2024, 4, 592−606

Author Contributions

CRediT: **Meng Song** investigation, methodology, writing-original draft; **Xiaoliang Zhang** investigation; **Shun Wan** investigation; **Gui Wang** investigation; **Junxiu Liu** investigation; **Weiwei Li** investigation; **Hongliang Dong** investigation; **Chenjie Lou** investigation; **Zhiqiang Chen** investigation; **Bin Chen** investigation; **Hengzhong Zhang** conceptualization, funding acquisition, supervision, writing-review & editing.

Notes

The authors declare no competing financial interest.

■ ACKNOWLEDGMENTS

This work was supported by the National Natural Science Foundation of China (grant no. 21875005). The authors thank Yanping Yang (HPSTAR) for help with SEM and TEM data collection.

■ REFERENCES

(1) Olabi, A. G.; Abbas, Q.; Al Makky, A.; Abdelkareem, M. A. Supercapacitors as next generation energy storage devices: Properties and applications. *Energy* **2022**, *248*, No. 123617.
(2) Choi, H. S.; Im, J. H.; Kim, T.; Park, J. H.; Park, C. R. Advanced energy storage device: a hybrid BatCap system consisting of battery–supercapacitor hybrid electrodes based on $Li_4Ti_5O_{12}$-activated-carbon hybrid nanotubes. *J. Mater. Chem.* **2012**, *22* (33), 16986–16993.
(3) Goodenough, J. B. Energy storage materials: A perspective. *Energy Storage Mater.* **2015**, *1*, 158–161.
(4) Prateek; Thakur, V. K.; Gupta, R. K. Recent progress on ferroelectric polymer-based nanocomposites for high energy density capacitors: synthesis, dielectric properties, and future aspects. *Chem. Rev.* **2016**, *116* (7), 4260–4317.
(5) Iro, Z. S.; Subramani, C.; Dash, S. S. A brief review on electrode materials for supercapacitor. *Int. J. Electrochem. Sci.* **2016**, *11* (12), 10628–10643.
(6) Gao, X.-P.; Yang, H.-X. Multi-electron reaction materials for high energy density batteries. *Energy Environ. Sci.* **2010**, *3* (2), 174–189.
(7) Fang, Y.; Zhang, J.; Xiao, L.; Ai, X.; Cao, Y.; Yang, H. Phosphate framework electrode materials for sodium ion batteries. *Adv. Sci.* **2017**, *4* (5), No. 1600392.
(8) Li, Y.; Lu, Y.; Zhao, C.; Hu, Y.-S.; Titirici, M.-M.; Li, H.; Huang, X.; Chen, L. Recent advances of electrode materials for low-cost sodium-ion batteries towards practical application for grid energy storage. *Energy Storage Mater.* **2017**, *7*, 130–151.
(9) Rost, C. M.; Sachet, E.; Borman, T.; Moballegh, A.; Dickey, E. C.; Hou, D.; Jones, J. L.; Curtarolo, S.; Maria, J.-P. Entropy-stabilized oxides. *Nat. Commun.* **2015**, *6*, No. 8485.
(10) Sarkar, A.; Wang, Q.; Schiele, A.; Chellali, M. R.; Bhattacharya, S. S.; Wang, D.; Brezesinski, T.; Hahn, H.; Velasco, L.; Breitung, B. High-entropy oxides: Fundamental aspects and electrochemical properties. *Adv. Mater.* **2019**, *31* (26), No. e1806236.
(11) Zeng, Y.; Ouyang, B.; Liu, J.; Byeon, Y.-W.; Cai, Z.; Miara, L. J.; Wang, Y.; Ceder, G. High-entropy mechanism to boost ionic conductivity. *Science* **2022**, *378* (6626), 1320–1324.
(12) Chen, J.; Liu, W.; Liu, J.; Zhang, X.; Yuan, M.; Zhao, Y.; Yan, J.; Hou, M.; Yan, J.; Kunz, M.; Tamura, N.; Zhang, H.; Yin, Z. Stability and compressibility of cation-doped high-entropy oxide MgCoNiCuZnO_5. *J. Phys. Chem. C* **2019**, *123* (29), 17735–17744.
(13) Bérardan, D.; Franger, S.; Dragoe, D.; Meena, A. K.; Dragoe, N. Colossal dielectric constant in high entropy oxides. *Phys. Status Solidi RRL* **2016**, *10* (4), 328–333.
(14) Bérardan, D.; Franger, S.; Meena, A. K.; Dragoe, N. Room temperature lithium superionic conductivity in high entropy oxides. *J. Mater. Chem. A* **2016**, *4* (24), 9536–9541.
(15) Sarkar, A.; Velasco, L.; Wang, D.; Wang, Q.; Talasila, G.; de Biasi, L.; Kübel, C.; Brezesinski, T.; Bhattacharya, S. S.; Hahn, H.; Breitung, B. High entropy oxides for reversible energy storage. *Nat. Commun.* **2018**, *9* (1), No. 3400, DOI: 10.1038/s41467-018-05774-5.
(16) Lin, X.; Salari, M.; Arava, L. M. R.; Ajayan, P. M.; Grinstaff, M. W. High temperature electrical energy storage: advances, challenges, and frontiers. *Chem. Soc. Rev.* **2016**, *45* (21), 5848–5887.
(17) Cho, Y.; Gabbar, H. A. Review of energy storage technologies in harsh environment. *Saf. Extreme Environ.* **2019**, *1*, 11–25.
(18) Chen, M.; Zhang, Y.; Xing, G.; Chou, S.-L.; Tang, Y. Electrochemical energy storage devices working in extreme conditions. *Energy Environ. Sci.* **2021**, *14* (6), 3323–3351.
(19) Hagoort, J. Prediction of wellbore temperatures in gas production wells. *J. Pet. Sci. Eng.* **2005**, *49* (1–2), 22–36.
(20) Moździerz, M.; Dąbrowa, J.; Stępień, A.; Zajusz, M.; Stygar, M.; Zając, W.; Danielewski, M.; Świerczek, K. Mixed ionic-electronic transport in the high-entropy $(Co,Cu,Mg,Ni,Zn)_{1-x}Li_xO$ oxides. *Acta Mater.* **2021**, *208*, No. 116735.
(21) Yan, J.; Zhang, L.; Liu, J.; Li, N.; Tamura, N.; Chen, B.; Lin, Y.; Mao, W. L.; Zhang, H. Pressure-induced suppression of Jahn–Teller distortions and enhanced electronic properties in high-entropy oxide $(Mg_{0.2}Ni_{0.2}Co_{0.2}Zn_{0.2}Cu_{0.2})O$. *Appl. Phys. Lett.* **2021**, *119* (15), No. 151901.
(22) van der Pauw, L. J. A method of measuring specific resistivity and Hall effect of discs of arbitrary shape. *Philips Res. Rep.* **1958**, *13*, 1–9.
(23) Newbury, D. E.; Ritchie, N. W. M. Is scanning electron microscopy/energy dispersive X-ray spectrometry (SEM/EDS) quantitative? *Scanning* **2013**, *35* (3), 141–168.
(24) Kasap, S. O. *Principles of Electronic Materials and Devices*, 4th ed.; McGraw-Hill: New York, NY, 2018; pp 412–443.
(25) Neamen, D. A. *Semiconductor Physics and Devices: Basic Principles*, 4th ed.; McGraw-Hill: New York, NY, 2003; pp 107–167.
(26) Kittel, C. *Introduction to Solid State Physics*, 8th ed.; John Wiley & Sons: New York, NY, 2005; pp 205–214.
(27) Liu, J.; Chen, J.; Li, W.; Tian, H.; Zhang, X.; Li, N.; Yan, J.; Kunz, M.; Chen, B.; Zhang, H. Differentiating the electrical and optoelectrical properties of oxysulfides $La_2Ta_2MS_2O_8$ (M= Zr, Ti) via application of pressure. *J. Phys. Chem. C* **2020**, *124* (27), 14477–14484.
(28) Lee, M. J.; Han, J.; Lee, K.; Lee, Y. J.; Kim, B. G.; Jung, K.-N.; Kim, B. J.; Lee, S. W. Elastomeric electrolytes for high-energy solid-state lithium batteries. *Nature* **2022**, *601* (7892), 217–222.
(29) Huggins, R. A. Simple method to determine electronic and ionic components of the conductivity in mixed conductors a review. *Ionics* **2002**, *8* (3), 300–313.
(30) Mezaki, T.; Kuronuma, Y.; Oikawa, I.; Kamegawa, A.; Takamura, H. Li-Ion Conductivity and Phase Stability of Ca-Doped $LiBH_4$ under High Pressure. *Inorg. Chem.* **2016**, *55* (20), 10484–10489.
(31) Huo, C.; Xu, K.; Ma, L.; Li, T.; Li, H.; Yang, X.; Kuang, X.; Liu, S.; Deng, S.; Chen, J. Colossal Ionic Conductivity in Interphase Strain-Engineered Nanocomposite Films. *J. Am. Chem. Soc.* **2023**, *145* (25), 13623–13631.
(32) Ruan, D.; Tan, L.; Chen, S.; Fan, J.; Nian, Q.; Chen, L.; Wang, Z.; Ren, X. Solvent versus Anion Chemistry: Unveiling the Structure-Dependent Reactivity in Tailoring Electrochemical Interphases for Lithium-Metal Batteries. *JACS Au* **2023**, *3* (3), 953–963.
(33) Nasir, M.; Park, J. Y.; Heo, P.; Choi, K. H.; Park, H. J. Li-La-Zr-O Garnets with High Li-Ion Conductivity and Air-Stability by Microstructure-Engineering. *Adv. Funct. Mater.* **2023**, *33* (35), No. 2303397.
(34) Wang, S.; Yan, M.; Li, Y.; Vinado, C.; Yang, J. Separating electronic and ionic conductivity in mix-conducting layered lithium transition-metal oxides. *J. Power Sources* **2018**, *393*, 75–82.
(35) Osenciat, N.; Bérardan, D.; Dragoe, D.; Leridon, B. C.; Holé, S.; Meena, A. K.; Franger, S.; Dragoe, N. Charge compensation mechanisms in Li-substituted high-entropy oxides and influence on Li superionic conductivity. *J. Am. Ceram. Soc.* **2019**, *102* (10), 6156–6162.

(36) Jensen, F. Activation energies and the Arrhenius equation. *Qual. Reliab. Eng. Int.* **1985**, *1* (1), 13−17.
(37) Han, T.; Liu, H.; Wang, J.; Gao, C.; Han, Y. Electrostrictive Effect of Materials under High Pressure Revealed by Electrochemical Impedance Spectroscopy. *J. Phys. Chem. C* **2021**, *125* (16), 8788−8793.
(38) Graham, R. A. Pressure dependence of the piezoelectric polarization of $LiNbO_3$ and $LiTaO_3$. *Ferroelectrics* **1976**, *10* (1), 65−69.
(39) Takamura, H.; Kuronuma, Y.; Maekawa, H.; Matsuo, M.; Orimo, S. Lithium ion conduction in lithium borohydrides under high pressure. *Solid State Ionics* **2011**, *192* (1), 118−121.
(40) Yoon, D. N.; Lazarus, D. Pressure Dependence of Ionic Conductivity in KCl, NaCl, KBr, and NaBr. *Phys. Rev. B* **1972**, *5* (12), 4935−4945.
(41) Samara, G. A. High-pressure studies of ionic conductivity in solids. *Solid State Phys.* **1984**, *38*, 1−80.
(42) Inaguma, Y.; Yu, J.; Shan, Y.-J.; Itoh, M.; Nakamuraa, T. The effect of the hydrostatic pressure on the ionic conductivity in a perovskite lanthanum lithium titanate. *J. Electrochem. Soc.* **1995**, *142* (1), L8.
(43) Tauc, J. Optical properties and electronic structure of amorphous Ge and Si. *Mater. Res. Bull.* **1968**, *3* (1), 37−46.
(44) Nilges, T.; Lange, S.; Bawohl, M.; Deckwart, J. M.; Janssen, M.; Wiemhöfer, H.-D.; Decourt, R.; Chevalier, B.; Vannahme, J.; Eckert, H.; Weihrich, R. Reversible switching between *p*- and *n*-type conduction in the semiconductor $Ag_{10}Te_4Br_3$. *Nat. Mater.* **2009**, *8* (2), 101−108.
(45) Guin, S. N.; Pan, J.; Bhowmik, A.; Sanyal, D.; Waghmare, U. V.; Biswas, K. Temperature dependent reversible *p-n-p* type conduction switching with colossal change in thermopower of semiconducting AgCuS. *J. Am. Chem. Soc.* **2014**, *136* (36), 12712−12720.
(46) Liu, F.; Yu, M.; Chen, X.; Li, J.; Liu, H.; Cheng, F. Defective high-entropy rocksalt oxide with enhanced metal−oxygen covalency for electrocatalytic oxygen evolution. *Chin. J. Catal.* **2022**, *43* (1), 122−129.
(47) Hsieh, P.-T.; Chen, Y.-C.; Kao, K.-S.; Wang, C.-M. Luminescence mechanism of ZnO thin film investigated by XPS measurement. *Appl. Phys. A: Mater. Sci. Process.* **2007**, *90* (2), 317−321.
(48) Chen, M.; Wang, X.; Yu, Y.-H.; Pei, Z.-L.; Bai, X.-D.; Sun, C.; Huang, R.-F.; Wen, L.-S. X-ray photoelectron spectroscopy and auger electron spectroscopy studies of Al-doped ZnO films. *Appl. Surf. Sci.* **2000**, *158* (1−2), 134−140.
(49) Grzesik, Z.; Smoła, G.; Stygar, M.; Dąbrowa, J.; Zajusz, M.; Mroczka, K.; Danielewski, M. Defect structure and transport properties in (Co, Cu, Mg, Ni, Zn) O high entropy oxide. *J. Eur. Ceram. Soc.* **2019**, *39* (14), 4292−4298.
(50) Kamaya, N.; Homma, K.; Yamakawa, Y.; Hirayama, M.; Kanno, R.; Yonemura, M.; Kamiyama, T.; Kato, Y.; Hama, S.; Kawamoto, K.; Mitsui, A. A lithium superionic conductor. *Nat. Mater.* **2011**, *10* (9), 682−686.
(51) Jun, K.; Sun, Y.; Xiao, Y.; Zeng, Y.; Kim, R.; Kim, H.; Miara, L. J.; Im, D.; Wang, Y.; Ceder, G. Lithium superionic conductors with corner-sharing frameworks. *Nat. Mater.* **2022**, *21* (8), 924−931.
(52) Wang, X.; Xiao, R.; Li, H.; Chen, L. Oxysulfide LiAlSO: a lithium superionic conductor from first principles. *Phys. Rev. Lett.* **2017**, *118* (19), No. 195901.
(53) Monchak, M.; Hupfer, T.; Senyshyn, A.; Boysen, H.; Chernyshov, D.; Hansen, T.; Schell, K. G.; Bucharsky, E. C.; Hoffmann, M. J.; Ehrenberg, H. Lithium diffusion pathway in $Li_{1.3}Al_{0.3}Ti_{1.7}(PO_4)_3$ (LATP) superionic conductor. *Inorg. Chem.* **2016**, *55* (6), 2941−2945.
(54) Buschmann, H.; Dölle, J.; Berendts, S.; Kuhn, A.; Bottke, P.; Wilkening, M.; Heitjans, P.; Senyshyn, A.; Ehrenberg, H.; Lotnyk, A.; Duppel, V.; Kienle, L.; Janek, J. Structure and dynamics of the fast lithium ion conductor "$Li_7La_3Zr_2O_{12}$. *Phys. Chem. Chem. Phys.* **2011**, *13* (43), 19378−19392.
(55) Thangadurai, V.; Weppner, W. $Li_6ALa_2Ta_2O_{12}$ (A= Sr, Ba): novel garnet-like oxides for fast lithium ion conduction. *Adv. Funct. Mater.* **2005**, *15* (1), 107−112.
(56) Slima, I. B.; Karoui, K.; Rhaiem, A. B. Ionic conduction, structural and optical properties of $LiCoO_2$ compound. *Ionics* **2023**, *29* (5), 1731−1739.
(57) Ma, S. B.; Kwon, H. J.; Kim, M.; Bak, S.-M.; Lee, H.; Ehrlich, S. N.; Cho, J.-J.; Im, D.; Seo, D.-H. Mixed Ionic−Electronic Conductor of Perovskite $Li_xLa_yMO_{3-\delta}$ toward Carbon-Free Cathode for Reversible Lithium−Air Batteries. *Adv. Energy Mater.* **2020**, *10* (38), No. 2001767, DOI: 10.1002/aenm.202001767.
(58) Wang, M. J.; Wolfenstine, J. B.; Sakamoto, J. Mixed electronic and ionic conduction properties of lithium lanthanum titanate. *Adv. Funct. Mater.* **2020**, *30* (10), No. 1909140.
(59) Wang, C.; Hong, J. Ionic/electronic conducting characteristics of $LiFePO_4$ cathode materials: The determining factors for high rate performance. *Electrochem. Solid-State Lett.* **2007**, *10* (3), A65.
(60) Pfeiffer, H.; Sánchez-Sánchez, J.; Álvarez, L. J. Lithium and tritium diffusion in lithium oxide (Li_2O), a molecular dynamics simulation. *J. Nucl. Mater.* **2000**, *280* (3), 295−303.

https://doi.org/10.1021/jacsau.3c00693
JACS Au 2024, 4, 592−606